Landslide-generated tsunamis at Réunion Island

Karim Kelfoun, Thomas Giachetti, Philippe Labazuy

Landslide–generated tsunamis at Réunion Island

Karim Kelfoun[1,2,3], Thomas Giachetti[1,2,3], Philippe Labazuy[1,2,3]

[1]Clermont Université, Université Blaise Pascal, Laboratoire Magmas et Volcans, Clermont−Ferrand
[2]CNRS, UMR 6524, F−63038 Clermont−Ferrand
[3]IRD, M 163, F−63038 Clermont−Ferrand

Abstract. Landslides that occur on oceanic volcanoes can reach the sea and trigger catastrophic tsunamis. Réunion Island has been the location of numerous huge landslides involving tens to hundreds of km^3 of material. We use a new two−fluid (sea water and landslide) numerical model to estimate the wave amplitudes and the propagation of tsunamis associated with landslide events on Réunion Island. A 10 km^3 landslide from the eastern flank of Piton de la Fournaise volcano would lift the water surface by about 150 m where it entered the sea. The wave thus generated would reach Saint−Denis, the capital of Réunion Island (population of about 150 000 people), in only 12 minutes, with an amplitude of more than 10 m, and would reach Mauritius Island in 18 minutes. Although Mauritius is located about 175 km from the impact, waves reaching its coast would be greater than those for Réunion Island. This is due to the initial shape of the wave, and its propagation normal to the coast at Mauritius but generally coast−parallel at Réunion Island. A submarine landslide of the coastal shelf of 2 km^3, would trigger a ~40 m−high wave that would severely affect the proximal coast in the western part of Réunion Island. For a landslide of the shelf of only 0.5 km^3, waves of about 2 m in amplitude would affect the proximal coast.

1. Introduction

Tsunamis have been extensively studied and experienced a renewed interest after the dramatic tsunami in Indonesia, on December 26th 2004, which revealed the vulnerability of coastal areas around the Indian Ocean and demonstrated the enormous damage that this type of cataclysm may produce [e.g. *Synolakis et al.*, 2008, the other references of this special volume and references therein]. The triggering of a tsunami originates either from large−scale earthquakes or from landslides [e.g. *Ward*, 2001; *Harbitz et al.*, 2006; *Fritz et al.*, 2008; *Waythomas et al.*, 2009]. The term 'landslide' is used here to describe all types of mass movements mobilizing rocks and soil by gravity. It encompasses the term 'debris avalanche' that we use to refer to the sudden and very rapid movement of an incoherent and unsorted mass [*Hoblitt et al.*, 1987] that reaches a long runout (> 10 km) and is generally of large volume (> 1 km^3).

The hot−spot volcano of Réunion Island is one of the largest volcanic edifices in the world, comparable to the Kilauea volcano (Hawaii) in size and in vertical accumulation of volcanic products (i.e. about 7 km from the oceanic floor). The formation of the island probably began about 5 My ago by the construction of underwater volcanic edifices that have been largely dismantled by huge flank collapses, and later re−covered by the more recent activity [*Oehler et al.*, 2007]. The Alizés volcano, on the submarine southeast part of the island, is one of these proto edifices. The present morphology of the island is essentially due to the evolution of the two more recent volcanic centers, the Piton des Neiges complex and the active volcano of the Piton de la Fournaise. The Piton des Neiges complex lies in the north−west part of the island and was built from about 2 My ago to about 12000 BP. Three large depressions, ~10 km wide and up to 2000 m deep (Figure 1), shape its morphology. A large number of outcrops in the depressions show deposits of numerous debris avalanches [*Oehler et al.*, 2007]. The explanation of the formation of the depressions is still in debate:

tectonic activity above underlying rift−zones, vertical subsidence of underlying dense rock complexes and scar formations by debris avalanches have been invoked [*Oehler et al.*, 2003; *Oehler et al.*, 2007; *Michon and Saint−Ange*, 2008; and references therein]. The Piton de la Fournaise volcano lies in the southeast part of the island. The present eruptive center is very active (1 to 2 eruptions per year on average). The edifice is cut by horse−shoe shaped structures that are interpreted to have been formed by eastward sliding [*Lénat and Labazuy*, 1990; *Labazuy*, 1996; *Merle and Lénat*, 2003], perhaps coupled with a subsidence component [*Michon*, 2007]. Recent measurements by radar interferometry agree with the eastward sliding hypothesis and show that the more recent structure, called the Grand Brûlé, is sliding eastward (*J.−L. Froger et al.*, manuscript in preparation, 2010).

Detailed bathymetric studies around the island have shown the presence of huge landslide submarine deposits. About 50 large−scale debris avalanche deposits in the last 2 My (*i.e.* one every 40000 years on average, a recurrence time that corresponds to the last events that affected the recent Piton de la Fournaise volcano), have been mapped (Figure 1) with volumes ranging from less than 1 to more than 1000 km^3 [*Labazuy*, 1996; *Oehler et al.*, 2004 ; *Oehler et al.*, 2007]. The last event would have occurred 4200 years ago [*Bachelery and Mairine, 1990*]. The present resolution of the bathymetry does not allow for the detection of events smaller than 1 km^3. Moreover, small events are easily covered by more recent deposits. It is thus probable that the recurrence time of smaller events is shorter than that deduced for huge events. *Keating and McGuire* [2000] identified not less than 23 processes that contribute to edifice collapse. The origin of the landslides observed at Réunion Island is still in debate and many processes could be invoked: pressure from the magmatic system, bulging, rock weakness through alteration, basal erosion by the sea, etc. (see *Oehler et al.* [2007] for more details). Large landslides of several cubic kilometers are potentially catastrophic tsunami generators [*Okal and Synolakis*, 2003] and the introduction of the

78 landslides mapped around Réunion Island into the ocean has certainly triggered tsunamis that
79 reached neighboring islands like Mauritius Island (about 175 km from Réunion Island). Some
80 of the rapid changes of sea level (up to 40 meters) observed in this area in the recent past and
81 the presence of several tens of cubic−meter reef blocks lying between 3 and 7 m above
82 present sea level [*Camoin et al.*, 2004] might have been brought about by tsunamis
83 originating from debris avalanches.

84 The majority of the population of Réunion Island and Mauritius live close to the shore.
85 The main cities, infrastructures, industries and airports are also located at low elevation and in
86 close proximity to the sea. We stress that slow sliding of the volcano, as inferred from the
87 horse−shoe shaped structures and from the radar interferometry [*Lénat and Labazuy*, 1990;
88 *Labazuy*, 1996; *Merle and Lénat*, 2003, *J.−L. Froger et al.*, manuscript in preparation, 2010]
89 does not mean that the movement will necessarily evolve into a debris avalanche. We also
90 stress that, to our present knowledge, huge landslides are very rare and that the risk they
91 represent is probably negligible on a human scale. However, it is now recognized that, on a
92 geological timescale, debris avalanches are common events for volcanoes that are on land or
93 are oceanic [*Moore et al.*, 1989; *Normark et al.*, 1993; *Holcomb and Searle*, 1991; *McMurtry*
94 *et al*., 2004] and we have no idea of the order of magnitude of the wave amplitude that would
95 be related to a landslide at Réunion Island, whatever the volume involved. The evaluation of
96 hazards related to these phenomena and to associated tsunamis has never been performed at
97 Réunion Island.

98 In the present study, we analyze the consequences of two kinds of potential landslides
99 using a new two−fluid numerical model. We first envisage a landslide of the recent part of the
100 island, on the eastern flank of the Piton de la Fournaise volcano, inside the Grand Brûlé
101 structure. We also discuss the consequences of a smaller submarine landslide that could
102 involve parts of the coastal coral reef shelf in the north western part of the island.

2. Models of landslide−generated tsunamis

Tsunami generation by landslides has already been studied using numerical simulations [e.g. *Heinrich et al.*, 1998; *Tinti et al.*, 1999, 2000, 2006a, 2006b; *Ward and Day*, 2001; *Waythomas and Watts*, 2003; *Waythomas et al*., 2009; *Geist et al*., 2009]. All the existing models applied to natural cases are 2D, and are often depth−averaged. One difference between the 2D models of water displacement is the way in which Navier−Stokes equations are approximated. For example, models based on the Boussinesq approximation allow wave dispersion to be taken into account (the velocity of the wave is dependent on its wavelength), whilst the shallow water approximation does not. The former is more accurate for the dynamics of waves whose wavelength is small compared to the water depth. For more details about the methods, the reader should refer to *de Saint Venant* [1871], *Boussinesq* [1872], *Wei et al*., [1995], *Watts et al*., [2000], *Harbitz et al*., [2006] and *Dutykh et Dias* [2007], amongst others.

Most of the previous models of landslide generated tsunamis do not simulate the underwater landslide propagation. Some models implicitly take it into account by imposing the initial shape of the water surface close to the impact [e.g. *Waythomas and Watts*, 2003; *Ioualalen et al.*, 2006]. This approach is motivated by the fact that the initial stages, at the point of impact, are often the most important for the wave generation (*Harbitz et al*., 2009) especially in the far field. However, it cannot take into account the effects of the dynamic behavior, or the shape of the landslide on waves generated. Other models consider the landslide as blocks moving with an imposed path, shape and velocity [e.g. *Tinti et al.*, 1999, 2000; *Ward and Day*, 2001; *Haugen et al.*, 2005]. Once again, the behavior of the landslide and its interaction with the underlying topography cannot be predicted. To improve the simulation, other authors (*Fryer et al*., 2004; *Tinti et al*., 2006a, b; *Waythomas et al*., 2006; *Waythomas et al*., 2009) simulate the landslide by calculating first the displacement of

discrete sliding blocks and, subsequently, the waves of water generated by these blocks. Other models consider both the landslide and the water as independent fluids. *Jiang and Leblond* [1992], for example, consider that the landslide behaves as a viscous flow. *Heinrich et al.* [1998] use a more complex numerical approach which integrates a 3D model close to the landslide−water impact in order to calculate the initial shape of the waves more accurately. Wave propagation is subsequently calculated using a classic 2D depth−average approach. The best approach would be a full 3D model with two fluids exhibiting not only density differences, as for *Heinrich et al.* [1998], but their own rheological behaviors in the whole calculation domain. However, computation times needed for such a code, as well as the lack of well constrained and defined rheological laws for submarine landslides, are currently limiting factors.

Our model simulates tsunami genesis by two fluids (landslide and water), which interact at each time step. The landslide influences the water and, in return, the water influences the landslide. The novelty of our approach is also that the scheme simulates the morphology and emplacement of the landslide using a rheological law calibrated through the comparison of the numerical results with natural deposits. The numerical model is based on the 2D depth−average approach, modified to incorporate the 3D interactions with greater accuracy.

3. Basic equations and rheologies

Both the landslides and sea water are simulated using the general shallow water equations of mass conservation and momentum balance. As shown later, the ratio of wave length to water depth of about 10 justifies this approximation [e.g. *Harbitz et al*., 2006]. The equations were solved using a modified version of the code *VolcFlow* that takes two fluids into account. The scheme is tested and presented in more detail in *Kelfoun and Druitt* [2005]

for one "fluid" (debris avalanche), where it successfully reproduces and explains the formation of all the first−order features (extension, thickness, levées, distal lobe, median escarpment) of the Socompa debris avalanche [*Kelfoun and Druitt*, 2005; *Kelfoun et al*., 2008]. The scheme used (the "double upwind scheme" described in *Kelfoun and Druitt* [2005]) limits the numerical dissipation of the velocity and allows for a good calculation of wave amplitudes even at large distances from the source.

3.1. Simulation of the landslide

The landslide is simulated by the following set of equations, where (1) and (2) are momentum balance and (3) is mass conservation:

$$\frac{\partial}{\partial t}\left(h_a u_x\right)+\frac{\partial}{\partial x}\left(h_a u_x^2\right)+\frac{\partial}{\partial y}\left(h_a u_x u_y\right)=g h_a \sin\alpha_x-\frac{1}{2}k_{act/pass}\frac{\partial}{\partial x}\left(g h_a^2\cos\alpha\right)+\frac{T_x}{\rho} \quad (1)$$

$$\frac{\partial}{\partial t}\left(h_a u_y\right)+\frac{\partial}{\partial y}\left(h_a u_y^2\right)+\frac{\partial}{\partial x}\left(h_a u_y u_x\right)=g h_a \sin\alpha_y-\frac{1}{2}k_{act/pass}\frac{\partial}{\partial y}\left(g h_a^2\cos\alpha\right)+\frac{T_y}{\rho} \quad (2)$$

$$\frac{\partial h_a}{dt}+\frac{\partial}{\partial x}\left(h_a u_x\right)+\frac{\partial}{\partial y}\left(h_a u_y\right)=0 \quad (3)$$

The variable h_a is the landslide thickness, ρ its relative density equaling the landslide density ρ_a (2000 kg m^{-3}) where the landslide is subaerial and ρ_a-ρ_w where it is submarine, and ρ_w being water density (see Table 1 for variables and units). The variable $\mathbf{u}=\left(u_x,u_y\right)$ is the landslide velocity, $k_{act/pass}$ the earth pressure coefficient (ratio of ground−parallel to ground−normal stress used with basal and internal friction angles, *Iverson and Denlinger* [2001]) and g is gravity. The ground slope is defined by α; α_x and α_y being the ground slope angles in the x−z and y−z planes respectively (x and y are the axes defined along the slope, z is the axis normal to the slope, see Kelfoun and Druitt [2005] for details). Other subscripts x and y denote the components of vectors in the x and y directions. The terms on the right−hand side

175 of the equations for momentum balance indicate, from left to right, the effect of the weight,
176 the pressure gradient and the total retarding stress, **T**.

177 The main difficulty in modeling landslide propagation is to define the total retarding
178 stress, **T**. Landslides exhibit a complex behavior that is at present impossible to describe
179 physically in a robust way. Moreover, in the case of submarine landslides, interactions
180 between landslide and water add complexity and probably involve mixing, dilution, water
181 infiltration, and density variations. Little is known about these mechanisms and how to
182 quantify them. It is important, however, to estimate the rheology since it controls the way the
183 landslide is emplaced, which directly influences the characteristics of the tsunami.

184 **T** can be first expressed as being the sum of $\mathbf{T}_{aw}$, the drag between the water and the
185 landslide, and of $\mathbf{T}_{ag}$, the stress between the landslide and the ground:

186 $$\mathbf{T} = \mathbf{T}_{aw} + \mathbf{T}_{ag} \quad (4)$$

187 The expression of $\mathbf{T}_{aw}$ is defined below in the section 3.3 “Interaction between landslide and
188 water”. In order to estimate $\mathbf{T}_{ag}$, we used morphological characteristics of past event deposits
189 (runout, width and width variations, form of the lateral edges and the front) and we tried to
190 reproduce these same characteristics numerically using various rheological laws, and by
191 varying the values of their parameters. Ten cases (Figure 1) have been used from submarine
192 data of *Oehler et al.* [2007], covering more than one order of magnitude in volume. Two main
193 conclusions can be drawn from the results of these simulations:

194 1) The Mohr−Coulomb frictional law (simply called frictional below) is often used in
195 granular flow dynamics, this law representing the behavior of deposits at rest and of sand
196 flows in the laboratory. The frictional retarding stress is defined by:

197 $$\mathbf{T}_{ag} = -\rho h \left(g\cos\alpha + \frac{\mathbf{u}^2}{r} \right) \tan\varphi_{bed} \times \frac{\mathbf{u}}{\|\mathbf{u}\|} \quad (5)$$

198 The best−fit value of the basal friction angle φ_{bed}, obtained by reproducing past events, ranges
199 from 3° to 5°, depending on the effect of the water (see section 3.4). However, if $\mathbf{T}_{ag}$ is
200 considered as a frictional law, it gives unrealistic deposits whatever the value of the friction
201 angles and the expression of $\mathbf{T}_{aw}$ chosen.
202 2) Considering $\mathbf{T}_{ag}$ as a constant retarding stress (i.e. constant whatever the thickness or
203 velocity of the landslide) generally gives better results. It allows for an approximate
204 reproduction of the extension, the thickness on all slopes and some morphological features
205 (levées, front) of natural deposits. Although difficult to explain from a physical point of view,
206 a similar conclusion has been obtained for subaerial debris avalanches [e.g. *Dade and*
207 *Huppert*, 1998; *Kelfoun and Druitt*, 2005; *Kelfoun et al.*, 2008]. Values of the best−fit
208 constant retarding stress describing the interactions between the ground and the landslide
209 depend on the stress exerted by the water. If the latter is considered as zero, $\mathbf{T}_{ag}$ ranges from
210 20 to 100 kPa, with a mean value of about 50 kPa. For a high retarding stress of the water (C_f
211 = 2, C_s = 0.01, see section 3.3), $\mathbf{T}_{ag}$ ranges between 10 and 50 kPa, with a mean value of about
212 20 kPa. It is, however, impossible to state if these ranges reflect variations of past event
213 rheologies or if they are related to the high uncertainties of the reconstructions: submarine
214 mapping, pre−landslide topography, estimation of sliding volumes, etc.
215

216 **3.2. Simulation of the water**

217 The water is simulated using a similar set of equations to those for the landslide:

218 $$\frac{\partial}{\partial t}\left(h_w v_x\right)+\frac{\partial}{\partial x}\left(h_w v_x^2\right)+\frac{\partial}{\partial y}\left(h_w v_x v_y\right)=g h_w \sin\beta_x-\frac{1}{2}\frac{\partial}{\partial x}\left(g h_w^2\cos\beta\right)+\frac{R_x}{\rho_w}-3\frac{\mu_w}{\rho_w h_w}v_x \quad (6)$$

219 $$\frac{\partial}{\partial t}\left(h_w v_y\right)+\frac{\partial}{\partial y}\left(h_w v_y^2\right)+\frac{\partial}{\partial x}\left(h_w v_y v_x\right)=g h_w \sin\beta_y-\frac{1}{2}\frac{\partial}{\partial y}\left(g h_w^2\cos\beta\right)+\frac{R_y}{\rho_w}-3\frac{\mu_w}{\rho_w h_w}v_y \quad (7)$$

220 $$\frac{\partial h_w}{dt}+\frac{\partial}{\partial x}\left(h_w v_x\right)+\frac{\partial}{\partial y}\left(h_w v_y\right)=0 \quad (8)$$

where β is the slope of the ocean bottom formed by the initial topography plus the landslide thickness calculated by equation (3). The water viscosity, μ_w, is fixed at 1.14×10^{-3} Pa s and ρ_w is water density, fixed at 1000 kg m^{-3}. The terms on the right−hand side of the equations for momentum balance indicate, from left to right, the effect of the weight, the pressure gradient, the drag between water and landslide and the drag between water and the ocean bottom.

To permit free propagation of waves, open boundaries are defined at the border of the domain by calculating the water velocity normal to the border, $v_{b,}$ from the water thickness h_w:

$$v_b = 2\left(c_1 - c_0\right) \quad (9)$$

where $c_1 = \sqrt{gh_w}$ and c_0 equals the value of c_1 at $t = 0$.

The water is able to interact with the bathymetry/topography and to flood onto the land. However, due to the shallow−water approach, waves breaking and other complex second−order 3D effects that occur at the shore are not taken into account. Sediment erosion and transport are also ignored. Since the main goal of this paper is to calculate an order of magnitude for the time of arrival, height and inland penetration of the waves, it is not essential to constrain these second−order effects.

3.3 Interaction between landslide and water

The two sets of equations (1−3 and 6−8) are calculated at the same time step and several assumptions rule the interactions between the two "fluids". The aim of our assumptions is to simplify the problem and to avoid the use of too many unconstrained parameters.

Firstly, we assume that no mixing between the landslide and ocean occurs and that the densities of the two fluids remain constant over time. This assumption precludes mixing between the landslide and the sea water, which could result in turbidity currents and affect the wave dynamics. It is supported by the observations of *Oehler et al*. [2007], who describe the

levées and front of the deposits as being more compatible with a homogenous flow emplacement, as for subaerial debris avalanches, than with turbidity deposits. Possibly the emplacement time is too short to allow water to penetrate deep into the landslide.

In our model, the landslide is affected by the water in two ways. Firstly, the reduced density of the landslide (ρ_a-ρ_w) is used where the landslide is underwater, with density ρ_a being used above the water. This reduces the driving forces and thus the velocity of the submarine flow. The second effect is related to $\mathbf{T}_{aw}$, the drag exerted by the water on the landslide. It is considered by some of the previous authors [e.g. *Tinti et al.*, 2006a] to depend on the surface of the landslide in contact with the water and on the square of the relative velocity of the landslide with respect to the fluid. For use in equations 1 and 2, the equations of *Tinti et al.* [2006a] have been rewritten as follows:

$$\mathbf{T}_{aw} = -\frac{1}{2}\rho\left(\tan\beta_{\mathrm{m}} C_{\mathrm{f}} + \frac{1}{\cos\beta_{\mathrm{n}}} C_{\mathrm{s}}\right) \left\|\mathbf{u}-\mathbf{v}\right\| \left(\mathbf{u}-\mathbf{v}\right) \tag{10}$$

where β_{n} is the angle formed by the intersections of both the surface of the landslide and the surface of the bathymetry with a plane normal to the displacement. The angle β_{m} is the slope of the landslide surface in the direction of the relative displacement and is given by:

$$\tan\beta_{\mathrm{m}} = -\nabla h_a \ \frac{\mathbf{u}-\mathbf{v}}{\left\|\mathbf{u}-\mathbf{v}\right\|} \tag{11}$$

The coefficients C_{f} and C_{s} fix the drag on the surface of the landslide respectively normal and parallel to the displacement. C_{f} and C_{s} both equal 0 outside the water. Underwater, C_{s} and C_{f} are greater than 0 where the scalar product of the relative velocity **u-v** by the outward normal vector **I** of the landslide surface is positive (i.e. where the landslide faces the direction of propagation), and is fixed to 0 elsewhere [*Tinti et al.*, 2006a]. Following previous studies [e.g. *Ward and Day*, 2001; *Tinti et al.*, 2006a; *Jiang and Leblond*, 1992], we assume that the water depth has no influence on the underlying landslide dynamics.

The water is displaced by the landslide in two ways. It can be accelerated by the displacement of the landslide (equations (6) and (7)). **R** thus equals -$\mathbf{T}_{aw}$ (equations (1) and (2)). This allows the landslide to "push" the water which is close to the shore. The transfer of momentum has a small effect on the velocity of the water at depth, where the mass of the landslide is small relative to the mass of the surrounding ocean. The second effect is due to the elevation of the base of the water by the landslide, which is expressed by a change of the basal slope β in equations (6) and (7). A direct combination of the two sets of equations, however, overestimates the amplitude of the waves generated. At a given point, a displacement of the landslide along the ocean floor induces a variation of its thickness h_a and thus a vertical displacement of the base of the water. This would induce the same variation of the sea level z_w, $\frac{\partial z_w}{\partial t} = \frac{\partial h_a}{\partial t}$, because an elevation of the base from equation (3) does not act directly on the water thickness of equations (6–8) but only lifts the water column (strictly speaking, it changes the basal slope, which has an equivalent effect). This is far from what is observed in reality. If, for example, a solid is introduced into a tank of water, the overall water surface is lifted by less than the height of the solid, and over a large surrounding area rather than just above the solid. This elevation is not related to a rapid flow of water initially lifted above the solid but is an immediate consequence of the onset of the impact.

This problem has already been discussed by several authors [e.g. *Sander and Hutter*, 1996; *Heinrich et al.*, 1998], and this is why *Heinrich et al.* [1998] used a full 3D calculation for where the landslide impacts the water. Other authors used an attenuation coefficient, $0 < \chi < 1$, which depends on a characteristic length of the slide and reduces the wave amplitude (e.g. *Tinti et al.* [2000]). The elevation of the sea surface is then calculated by:

$$\frac{\partial z_w}{\partial t} = \chi \frac{\partial h_a}{\partial t} \qquad (12)$$

However, if the characteristic length can be defined for a landslide when it is considered as a non−deformable block, it is much more difficult to define if this landslide spreads with time, changes in shape and presents strong velocity variations. Another problem is that equation (12) implies that the water column thickness is artificially reduced and that mass conservation is not respected. Finally, for a rigid block, the water is only lifted above it and not over a large area surrounding the impact.

To address this problem, we have chosen to calculate the surface elevation induced by a sudden displacement at the ground using a 3D model. Then we have determined the 2D mathematical expression of this surface elevation by fitting to the 3D results. This avoids the prohibitive computational time of a 3D approach along the 50 km−long interaction between the water and the landslide.

In the 3D model, the water is considered as being incompressible and surface elevation is calculated by mass conservation:

$$\nabla \mathbf{v} = 0 \tag{13}$$

Here only, the water velocity is defined in 3D: $\mathbf{v} = \left(v_x, v_y, v_z\right)$. This 3D−model reproduces a sudden elevation of the water all around a basal displacement rather than just above it (Figure 2).

If the bottom is a horizontal plane, the sudden elevation of the water calculated by solving equation (13) is fitted by:

$$\Delta z = c \times \frac{V}{d^2} \times e^{-\ln(\pi) \times d / h_w} \tag{14}$$

where V is the volume displaced vertically at the bottom, c is a parameter that allows mass conservation in order that $\int_{x=-\infty}^{\infty} \int_{y=-\infty}^{\infty} \Delta z dx dy = V$, and $d = \sqrt{x^2 + y^2 + h_w^2}$ is the distance between a given point (x, y, h_w) of the water surface and the point at the bottom (x = 0, y = 0, z = 0) where volume change occurs. Δz is assumed to equal zero where there is no water. Figure

316 2a indicates cross−cut profiles of the elevation obtained by 3D−simulations and by equation
317 (14) for a bottom located at h_w = 25, 50 and 100 m beneath the sea surface. The uplift is 1 m
318 and affects a 1 m² surface (volume displaced is 1 m^3).

319 Equation 14 fits exactly for a horizontal base and is thus well suited to a landslide on
320 the ocean floor. It is less good in the vicinity of steep slopes and close to the shore, but still
321 fits correctly (Figure 3b). It should be noted, therefore, that without correction the uplift of the
322 base would affect 1 m^2 of the water surface and would lift it 1 m in amplitude. Also note that
323 the 45° slope used in the simulation is an extreme case as the underwater slopes around
324 Réunion Island are less than 20°.

325 For a change of volume locally, the difference between the direct coupling and
326 correction appears to be very great (4 to 5 orders of magnitude, Figure 2). However, this
327 effect is much more limited for a large landslide and where the interactions are long term
328 because stacking all the surface elevations generated by each point of the landslide may give a
329 similar thickness at the centre of the landslide to that with no correction.

330

331 **3.4 Numerical resolution of water / landslide interactions**

332 Numerically, at each time step d*t*, the displacement of the landslide is first computed
333 (equations (1−3)), taking into account the water velocity of the previous time step, which is
334 chosen to be small enough to consider velocity variations during the time step as negligible (<
335 0.1 s). The effect of each variation of the landslide thickness, dh_a, on the water surface
336 elevation is then calculated using equation (14) to reduce wave amplitude taking more
337 accurately into account the 3D effects. Lastly, the water dynamics are computed by equations
338 (6− 8) using, if needed, the acceleration caused by the stress of the landslide and computed by
339 equation (10).

340

3.5 Tests of sensitivity

The rheology of the landslide and the stress caused by the water are not accurately constrained. To test the sensitivity of results on assumption done, we have performed simulations varying the following parameters (Table 2).

Simulations were done with C_f and C_s fixed to 2 and 0.01 respectively, following *Tinti et al.* [2006a]. Other simulations were done with the end member case where the water does not exert any stress on the landslide (C_f and C_s both fixed to 0, the reduced density only affecting the landslide velocity). We also simulated cases where coefficients C_f and C_s were fixed to 1 and 0.005 respectively. Depending on the values chosen, a mean value of $\mathbf{T}_{ag}$ = 20 kPa, 50 kPa and 35 kPa respectively allowed the landslide runouts to be reproduced using a constant retarding stress rheology.

We also performed simulations with the commonly−used Mohr−Coulomb rheology. The best−fit value of the basal friction angle, φ_{bed}, obtained by reproducing past events, is about 5° if C_f and C_s both equal 0, and 3° if they equal 2 and 0.01 respectively. Since the internal angle has a minor influence on the simulations, we only present here results obtained with internal isotropic stresses (*i.e.* no internal friction angle, $k_{act/pass}$ = 1, equations (1−2)).

Finally simulations were performed in which the energy lost by the landslide is entirely transferred, as momentum, to the water: $\mathbf{R} = -\mathbf{T}$. The stress $\mathbf{R}$ has also been artificially fixed to 0 to take into account that all the mechanical energy is transformed into heat in the water (50% to nearly 100% can be lost according to *Ruff* [2003]).

Other variations related to specific scenarios are discussed below.

4. Scenarios envisaged

4.1. Landslide from the active edifice

We first envisage a landslide on the eastern flank of the Piton de la Fournaise volcano (Figure 4). Following previous studies [*Labazuy*, 1991; *Merle and Lénat*, 2003] the geometry of the sliding zone has been defined from morphological evidence: ramparts and headwalls of the *Grand Brûlé* caldera to the north and south, with an underwater break in slope to the east. The base of the sliding zone has been defined from a geothermal borehole that shows the existence of gliding interfaces [*Rançon*, 1990; *Labazuy*, 1991]. Two landslide volumes were tested, the western boundary of the collapse being defined respectively by (1) the break in slope of the *Grandes Pentes* and (2) the summit crater. The volumes of these areas are respectively 10 km^3 and 25 km^3, which is in the order of magnitude of the more recent debris avalanche deposits mapped by *Oehler et al.* [2007]. For each case the landslide was simulated both as a single event and as three retrogressive landslides of the same volume (3.3 km^3 and 8.3 km^3, each landslide being separated by one minute).

Height scenarios are presented in Table 2 for the landslide of the active edifice. The varying parameters are the volume of the landslide, the type of landslide (single event, retrogressive), the rheological model of the landslide (frictional, constant), the value of the rheological parameters, the value of the drag of the water and whether or not the energy lost by the landslide through water drag is dissipated as heat or fully transferred to the water.

4.2. Submarine landslide of the coastal shelf

In the second scenario, we envisage what would occur in the case of a landslide of the coastal shelf, corresponding to the transition between subaerial and submarine environments. The shelf is well developed in the northwestern region, adjacent to the St−Paul (Figure 1) area, where it is bounded by 250 m−high cliffs. Here the coastal shelf is composed of a coral

reef plateau built on old, unstable landslide deposits and river fan sediments. Its boundaries probably correspond to a paleocoastline related to eustatic sea level variations [*Oehler et al.*, 2007]. Large landslides of the shelf, several cubic kilometers in volume, were mapped by *Oehler et al*. [2007]. Smaller landslides probably occurred too, but, because of their small volumes, they are easily eroded and/or covered by other deposits, and both their detection and estimation of recurrence times are difficult since the imagery data available (sonar, seismic) are not accurate enough to observe their form in detail. It is thus difficult to check if the rheology obtained for larger landslides is suitable for the simulation of smaller events (<1 km^3), but we assume here that their rheologies are similar. However, as for landslides of the active edifice, other rheologies were tested.

We tested three examples of landslides, one with a large volume of 2 km^3 to the west of the shelf, and two with smaller volumes of 0.5 km^3 and 0.1 km^3 to the north.

4.3. Bathymetry and topography used

The digital elevation model (DEM) was obtained by combining our data of the local bathymetry, ETOPO2 data for the regional bathymetry and Shuttle Radar Topography Mission (STRM) data for the aerial topography. The resolution is 200 m × 200 m, the regional simulations being performed on a 400 m × 400 m−resolution DEM in order to limit calculation time.

5. Results

5.1. Landslide from the active edifice – scenario 1

Numerical results presented here were calculated using a volume of 10 km^3, in a single event landslide, values of C_s = 0.01 and C_f = 2 and a constant retarding stress rheology of 20 kPa (scenario 1, Table 2). Other results are presented in the following section.

The simulated landslide of scenario 1 spreads eastwards and then splits up into two major lobes due to a topographic high facing the scar (Figure 5a). The northern lobe then divides into three lobes that follow the bathymetric depressions. The landslide reaches a maximum distance of ~45 km to the northeast at a mean velocity of ~45 m s^{-1}. Each lobe of the deposit has a mean thickness of between 10 to 20 m, the thickness increasing downstream from 10 m at the scar to 60 m close to the front.

Where the landslide enters the sea, it pushes and lifts the water surface 150 m above the initial sea level. A giant wave then propagates, hugging the shoreline of Réunion Island (Figure 6). It severely affects the east coast, with wave amplitudes that could exceed 100 m. The amplitude (Figure 7) remains high (> 50 m) along the northeast and southeast coasts of the island, within sight of the location of the wave formation, locally reaching 100 m where waves reflected by the bathymetry superimpose themselves. Highest water amplitudes and penetration of seawater inland occurs locally where the coast is perpendicular to the direction of propagation, allowing the wave to strike the island frontally. The low area of Saint−André, on the northeastern part of the island, is in this configuration and the water runs several km inland.

The amplitude decreases rapidly around to the southern and northern shores, the shape of the island protecting these areas from waves arriving normal to the coast. The area of St Pierre, to the south, is affected by a > 10−m wave approximately 10 minutes after the landslide (Figures 6a and 8a, Table 3−4). A second wave of ~30 m, formed by the reflux of the sea into the landslide scar, reaches the area five minutes later. The first wave reaches the main city of the island, Saint−Denis, 12 minutes after the onset of the landslide with an amplitude of nearly 10 m and the second wave, > 25 m in amplitude, after 18 minutes (Figure 8a, Table 3−4). Le Port, which is located to the northwest, on the opposite side of the island to the landslide, is one of the last places affected by the tsunami, after 15 minutes. This

441 northwestern coast is protected by the shape of the island and is affected by waves less than
442 5−m in amplitude (Figure 8a). However, waves are amplified by the superposition of the two
443 groups of waves encircling the island, one coming from the south, the other from the north
444 (Figure 6b).

445 To the east, the tsunami propagates out into the deep ocean and its amplitude
446 decreases due to the radial dissipation of the energy (Fig. 7). But, 150 km to the northeast of
447 the impact, the water depth decreases around Mauritius: the tsunami slows down and,
448 consequently, increases in amplitude. Waves of more than 40 m hit the southern part of the
449 island 18 minutes after the tsunami genesis (Figures 6b, 8b). Locally, due to the shape of the
450 island, reflections produce amplitudes that can exceed 100−m. The capital, Port−Louis, in the
451 northwest, and the airport, in the southeast, are affected by waves greater than 20 m in
452 amplitude. Waves of less than 10 m (except scenario 7, 18.5 m, 25 km^3) are recorded in the
453 northeast of Mauritius. The inland penetration is also further (~ 5 km) for Mauritius than for
454 Réunion Island because of the low−lying topography of the island. About 10−15% of the
455 island would be inundated by water.

456 The waves reflected off the Mauritius coast move back to Réunion Island. According
457 to the model, these waves hit the northeast coast of Réunion Island frontally, reaching an
458 amplitude higher than those of the first waves. They reach St Denis about 45 minutes after the
459 landslide (at 2700 s in Figure 8a).

460 In the Indian Ocean, the amplitude of the waves decreases exponentially away from
461 the island (Figure 7). The highest amplitudes are recorded to the east of the landslide, still
462 reaching 40−m at 100 km (Figure 7). To the west, the amplitudes are very low, less than 5 m
463 at some kilometers from the coast (Figures 7 and 8c).

464

465

5.2. Landslide from the active edifice – other scenarios

The transmission of the momentum lost by the avalanche to the water has minor consequences on the results obtained (scenarios 1 and 2, Table 2). It only increases the velocity and the wave amplitude close to the shore but its effect is small compared to the uplift of the water. The effect of momentum transmission is difficult to predict a priori. It increases the velocity of the water where the landslide enters the sea and thus the wave amplitude in the ocean facing the landslide, but it also changes the wavelength. Along the coast, where the wave amplitudes increase together with a shortening of the wavelengths, and where wave interactions are high due to reflections, the waves are sometimes higher, sometimes lower than if no transmission of the momentum were calculated. The feedback effect on the landslide is negligible, the mass of the landslide not being sufficient to significantly accelerate the huge mass of surrounding water.

The effect of C_s and C_f (scenarios 1, 3 and 4) is to reduce the velocity of the landslide when it is underwater, the front being strongly affected by C_f. The mass of the landslide then accumulates behind the front, forming a flow thick enough to overflow into depressions bordering the main channel. Lowering this value accelerates and thins the landslide, resulting in the deposits being more channelized. In the extreme case, where C_s and C_f are both considered as 0, the deposits are mainly concentrated in 2 lobes (Figure 5b). They are bordered by 20 to 40 m thick levées and are thicker at the front. This morphology appears closer to natural deposits than with high values of C_s and C_f. The very high mean velocity of 80 $m.s^{-1}$, with a maximal velocity of more than 100 $m.s^{-1}$, forms deposits within sight of the scar, and which are less spread out.

If the landslide is considered as frictional, with $C_f = 2$ and $C_s = 0.01$, a basal friction of 3° is needed to fit the runout of past events (scenario 6). The landslide deposits are spread out (Figure 5c), have very thin edges, a thick mass locally and do not show any levées or a well

491 marked front. If C_s and C_f both equal 0, the best fit friction angle is 5° (scenario 5). Deposits
492 formed are widely dispersed (Figure 5), covering an area of about 2000 km². Simulated
493 deposits with the frictional model have less of a resemblance to the deposits mapped by
494 *Oehler et al.* [2007] than those produced with the constant retarding stress model.

495 Although different in the near field, the overall times of arrival and tsunami kinematics
496 obtained for all scenarios with the same volume of 10 km^3 released in a single episode are
497 close to those described in the previous section (Table 3−4). The initial wave amplitude may
498 change but the same volume of water is displaced over a similar period of time. For example,
499 with the frictional model (scenario 5), the wider spread landslide generates smaller wave
500 amplitudes (Figure 9b) but with larger wavelength. Where the tsunami reaches the coast,
501 wavelengths decrease and amplitudes increase to reach amplitudes of more than 50 m (about
502 100 m locally), the order of magnitude of waves obtained with the constant retarding stress
503 (Figure 9a, Table 3).

504 Wave amplitude obviously depends on the way the mass slides and the volume that
505 impinges on the sea. Should the same landslide volume of 10 km^3 move by retrogressive
506 failures, or by slow sliding, waves 3 times smaller would be formed (however, deposits
507 formed by scenarios 1 and 8 are very similar). In a more catastrophic scenario, which
508 envisages that all of the Grand Brulé scar (between the summit and the sea, Figure 4) slides
509 rapidly as a single mass (25 km^3), waves could reach 2−3 times the amplitude previously
510 shown for the 10 km^3 case (scenario 7, Table 2−4).

511

512 **5.3. Submarine landslide of the coastal platform**

513 The larger landslide in the west (Figure 10a) induces waves of about 20−30 m in
514 amplitude that affect about 40 km of the neighboring shore. Waves of more than 10 m in
515 amplitude form locally along about 50 km of the shoreline, but the amplitude decreases

rapidly, reaching less than 2 m 30−40 km from the landslide. The 0.5 km^3 landslide to the northeast (Figure 10b) affects the adjacent 10 km of shoreline with waves higher than 20 m (40 m locally). However, the zone affected by smaller waves is more limited than in the previous case. For both larger landslides, the sea water penetrates more than 2 km inland, into the flat−lying area of Saint−Paul. In the case of the ~ 0.1 km^3 volume landslide (Figure 10c), the resulting waves are only about 3 m−high along 20 km of the proximal coast. Their effects are negligible (<0.2 m) at 30 km from the landslide and they are unable to penetrate inland.

The wave is positive in all areas facing the landslide. Behind the landslide, the first wave is negative: the water level decreases for about 2 minutes before the arrival of the first positive wave. Due to the proximity of the potential landslide area (less than 10 km from the shoreline), waves reach the coast in less than 2 minutes.

6. Discussion

The occurrence of landslides of several cubic kilometers only occur at Réunion Island on a geological timescale, and are very scarce on a human timescale. This sparcity of events explains why it is very difficult to validate any numerical model of these exceptional phenomena using field data due to the lack of direct observations. It is also impossible to measure the rheology and to quantify accurately interactions between the landslide and water. This problem of validation, however, also highlights the purpose of numerical simulations, which give an idea of the wave amplitude that such landslides could cause. Of course, uncertainties remain, due to the assumptions and simplifications implicit in the model and in the rheological behaviors chosen. In addition, the rheology we have chosen through the simulation of past events is not fully understood. However, this law seems to be able to capture the first order behavior of this kind of complex flow and to form numerical deposits with levées, lobes, and thicknesses which appear to be in good accordance with the

morphological features of the older deposits mapped by *Oehler et al*. [2007]. Note that the value used for the retarding stress, 20 kPa, with $C_f = 2$ and $C_s = 0.01$ (50 kPa if $C_f = 0$ and $C_s = 0$), is approximately half of the ~50 kPa mean value of *Dade and Huppert* [1998], and of the stress obtained by *Kelfoun and Druitt* [2005] for the subaerial Socompa avalanche. The main part of the emplacement being underwater, the same ratio is observed between the relative density used underwater (1000 kg m^{-3}) and subaerial density (2000 kg m^{-3}). The value of the constant retarding stress might then be implicitly related to the density of the landslide and thus to the internal stresses that are related to its weight.

Overall, the greatest uncertainties are linked to the scenario chosen: how does the mass slide? What is the destabilized volume? This is why our aim is not to forecast the effect of a hypothetical landslide on Réunion Island, but to estimate the magnitude of the waves that could be produced, to determine the time before wave arrival and to characterize the dynamics of the tsunami, should a landslide occur here. It is also why we have simulated landslides which differ in volume (0.5, 1, 2, 10, 25 km^3), rheology, drag of water, landslide location and way of collapsing (in one go or by retrogressive failures).

Simulations of the landslide from the active edifice show that waves as high as 100 m in amplitude could affect the coasts of Réunion Island and Mauritius if volumes greater than 10 km^3 are involved. It also enables the kinematics of such an event to be predicted, and the effects of the topography / bathymetry on the wave amplitude and dynamics to be quantified. For example, for all scenarios envisaged, the southwestern coast of Mauritius Island, located at 175 km from the impact, is more affected by the tsunamis than the Réunion coastline itself due to the dynamics explained in the results section.

In the deep ocean, the amplitude of the waves decreases progressively eastwards, reaching about 20 m at 250 km from the impact (east boundary of the calculation grid, Figure 7). Extrapolation of the wave amplitude further out into the deep ocean to the east gives < 1

mm waves at 2 000 km from the impact whatever the type of extrapolation chosen. Even though wave amplitude increases as the water depth decreases, the effect on the Australian coasts, the first land encountered by the tsunami, more than 5500 km from the impact, appears to be negligible.

To the west, the wave amplitude becomes negligible closer to the island, because the latter protects this sector from the initial wave (Figure 8c). Madagascar, 750 km to the west of Réunion Island, would thus be little affected by a landslide from the Piton de la Fournaise. Waves generated by a 2 km^3 landslide of the coastal shelf (Figure 10 a−b) are smaller than for a landslide of the volcano itself because of the smaller volume involved, but also because of the slow velocities and small runout of the landslide. The driving forces are reduced by the effect of the water in a submarine environment and the submarine slides do not experience subaerial acceleration. The less steep geometry of the coastal shelf also generates lower velocities and smaller runout. Increasing the velocity and runout of the landslide, by changing the rheological model or lowering the value of the constant retarding stress, would generate slightly higher waves, but their amplitude is always <40 m and the effect is local (covering 50 km of the coastline), the bathymetry playing a fundamental role in the dynamics. The waves are also restricted to a limited portion of the shore due to the form of the bay facing the coastal shelf that protects the more distant shores from direct impact of the tsunami.

The tsunami hazard associated with a landslide event on Réunion Island would thus be dramatic on a local scale (proximal shore for a landslide of the shelf, shores of Réunion Island and Mauritius for a large landslide of the active part of the volcano), but small on a regional scale. This is mainly because the wave generation is localized to a relatively small area of several tens of square kilometers and because the energy dissipates rapidly in a radial manner.

If wave amplitude is the main parameter, the evacuation time should also really be taken into account for hazard assessment. This evacuation time is long enough for the case of

a tsunami triggered by huge seismic shock occurring at the opposite side of the Indian Ocean (as in the 26 December 2004 case). It would, however, be very short for Réunion coasts in the case of a landslide on or around the island: less than 2 minutes to reach the nearest coast for a coastal landslide, 10 to 20 minutes depending on the landslide volume for the wave to encircle the island, 10 to 30 minutes to reach Mauritius Island.

The amplitudes of 100 m for the large landslide may intuitively appear huge but they are, however, compatible with the enormous volumes (10 km^3) chosen to slide. Waves are ~10 times higher than that generated following the collapse of Stromboli in December 2002: a 10 m−high wave was formed [*Maramaï et al.*, 2005], but the landslide was only 17.10^6 m^3, 500 times smaller than the volume tested in our simulation. The wave generated by the Lituya bay landslide (volume of 30.10^6 m^3; 300 times smaller than our volume), in Alaska in 1958 [*Miller*, 1960; *Fritz et al.*, 2001] propagated into the bay, reaching 500 m close to the impact, 60 m laterally at 6 km from the collapse and 30 m at 12 km. Even if we cannot make a direct comparison between the case of Lituya Bay, in which water was channeled by the bay, and our case in which waves propagate in the open sea, this example also supports the fact that our amplitudes and times are realistic. In Hawaii, waves as high as 300 m, originating from debris avalanches, are believed to have affected the islands in the past [e.g. *Moore and Moore*, 1984, 1988].

7. Conclusion

Our simulations use a rheological behavior for the landslide which is compatible with real deposits and allows for the estimation of wave amplitudes, times of wave arrival and inland penetration with the limitation of the approach used. They give a new insight into the risk assessment at Réunion Island and Mauritius. On a geological timescale, these islands may be hit by huge tsunamis which could cause disaster for superstructures and inhabited areas

located on or near the destabilized areas, not to mention the possibility of the direct impact on the shorelines, where hundreds of thousands of people live, and on the main social infrastructures. For example, Réunion Island airport is close to the sea, at an elevation of 5 m, and the main road is located between 5 and 10 m above sea level.

However, to our present knowledge, the frequency of large landslides at Réunion Island is approximately 1 every 40000 years on average. The magnitude of such events would be catastrophic, but hazard (magnitude × occurrence) is very low because of the very low recurrence time.

On a human timescale, the most pertinent events are the small−volume landslides. These landslides are smaller but more frequent. Their effect would only be local but could cause damage and fatalities and could be very devastating for harbor infrastructures. Due to their small size, small event deposits (<1 km^3) are difficult to detect, are easily eroded and rapidly covered by more recent deposits, resulting in the underestimation of their recurrence. An effort to carry out high−resolution underwater mapping should be made to estimate more accurately the frequency of such landslides. The results presented here also reinforce the necessity to set up a local alert network (wave amplitude, deformation, seismic) to forecast such events. However the evacuation time would be very short for Réunion coasts in the case of a landslide around the island. Forecast strategies for subaerial and submarine landslides thus need to be developed on Réunion Island, but also on most other oceanic islands that show huge landslide deposits, such as the Canary Islands [*Ablay and Hürlimann* 2000; *Krastel et al.* 2001; *Ward and Day*, 2001; *Masson et al.* 2002] or the Hawaiian Islands [Moore et *al.*, 1989, 1994].

Acknowledgements

Those studies have been funded by the French *Centre national de la recherche scientifique* (CNRS) and by the *Institut de Recherche pour le Développement* (IRD). We thank Ariel Provost for his help in the

formulation of the equations. The paper was improved by Fran van Wyk de Vries and by the very useful comments of three anonymous reviewers and the Editors.

References

Ablay, G., and M. Hürlimann (2000), Evolution of the north flank of Tenerife by recurrent giant landslides, *J. Volcanol. Geotherm. Res.*, *103*, 135–159.

Bachelery, P., and P. Mairine (1990), Evolution volcano−structurale du Piton de la Fournaise depuis 0.53 M.a., in *Le volcanisme de la Réunion, monographie*, edited by J.−F. Lénat, pp. 213−242, Clermont−Ferrand.

Boussinesq, J. (1872), Théorie des ondes et des remous qui se propagent le long d'un canal rectangulaire horizontal, en communiquant au liquide contenu dans ce canal des vitesses sensiblement pareilles de la surface au fond, *J. Math. Pures Appl.*, *17*, 55–108.

Camoin, G., L. Montaggioni, and C. Braithwaite (2004), Late glacial to post glacial sea levels in the Western Indian Ocean, *Mar. Geol.*, *206*, 119–146.

Dade, W. B., and H. E. Huppert (1998), Long−runout rockfalls, *Geology*, *26*, 803–806.

de Saint−Venant, A. J. C. (1871), Théorie du mouvement non−permanent des eaux, avec application aux crues des rivières et à l'introduction des marées dans leur lit, *C. R. Acad. Sc. Paris, 73,* 147–154.

Dutykh, D., and F. Dias (2007), Dissipative Boussinesq equations,*C.R. Mecanique, 335*, 559–583. Special issue dedicated to J. V. Boussinesq, doi: 10.1016/j.crme.2007.08.003.

Fritz, H. M., W. H. Hager, and H. E. Minor (2001), Lituya Bay case: rockslide impact and wave run−up, *Sci. Tsunami Hazards*, *19*(1), 3–22.

Fritz, H. M., N. Kalligeris, J. C. Borrero, P. Broncano, and E. Ortega (2008), The 15 August 2007 Peru tsunami runup observations and modeling, *Geophys. Res. Lett.*, 35, L10604, doi:10.1029/2008GL033494.

Geist, E.L., J. L. Patrick, D. C. Jason (2009), Hydrodynamic modeling of tsunamis from the Currituck landslide, Marine Geology 264 (2009) 41–52, doi:10.1016/j.margeo.2008.09.005.

Harbitz, C.B., F. Løvholt, G. Pedersen, and D.G. Masson (2006), Mechanisms of tsunami generation by submarine landslides: a short review, *Norweg. J. Geol., 86*, 255–264.

Haugen, K. B., F. Lovholt, and C.B. Harbitz (2005), Fundamental mechanisms for tsunami generation by submarine flows in idealised geometries, *Mar. Petr. Geol.*, *22*, 209–217.

Heinrich, P., A. Mangeney, S. Guibourg, and R. Roche (1998), Simulation of water waves generated by a potential debris avalanche in Montserrat, Lesser Antilles, *Geophys. Res. Lett.*, *25*, 3697–3700.

Hoblitt, R. P., C. D. Miller., and W. E. Scott (1987), Volcanic Hazards with Regard to Siting Nuclear−Power Plants in the Pacific Northwest, *USGS Open−File Report*, 87−297.

Holcomb, R. T., and R. C. Searle (1991), Large landslides from oceanic volcanoes, *Mar. Geotech., 10*, 19–32.

Ioualalen, M., B. Pelletier, P. Watts, and M. Regnier (2006), Numerical modeling of the 26 November 1999 Vanuatu tsunami, *J. Geophys. Res.*, *111*, C06030, doi:10.1029/2005JC003249.

Iverson, R. M., and R. P. Denlinger (2001), Flow of variably fluidized granular masses across three−dimensional terrain: 1. Coulomb mixture theory, *J. Geophys. Res.*, *106*, 537– 552.

Jiang, L., and P.H. LeBlond (1992), The Coupling of a Submarine Slide and the Surface Waves which it Generates, *J. Geophys. Res. 97 (C8)*, 12,731−12,744.

Keating, B. H., and W.J. McGuire (2000), Island Edifice Failures and Associated Tsunami Hazards, *Pure appl. geophys. 157*, 899–955.

Kelfoun, K., and T.H. Druitt (2005), Numerical modelling of the emplacement of Socompa rock avalanche, Chile, *J. Geophys. Res.*, *110*, B12202.

Kelfoun K., T.H. Druitt, B. van Wyk de Vries, and M.–N. Guilbaud (2008), Topographic reflection of Socompa debris avalanche, Chile, *Bulletin of Volcanology, 71 (9)*, 1057−1075. DOI: 10.1007/s00445−008−0201−6.

Krastel, S., H. U. Schmincke, C. L. Jacobs, R. Rihm, T.M. Le Bas, and B. Alibés (2001), Submarine landslides around the Canary Islands, *J. Geophys. Res.*, *106*, 3977–3997.

Labazuy, P. (1991), Instabilités au cours de l'évolution d'un édifice volcanique en domaine intraplaque océanique : Le Piton de la Fournaise (Ile de Réunion Island), PhD thesis, 260 pp, Univ. Blaise Pascal, Clermont−Ferrand, 11 July.

Labazuy, P. (1996), Recurrent landslides events on the submarine flank of Piton de la Fournaise volcano (Reunion Island), *Geol. Soc. London*, *110*, 293–305.

Lénat, J.−F., and P. Labazuy (1990), Morphologies et structures sous−marines de la Réunion, in *Le volcanisme de la Réunion, monographie*, edited by J.−F. Lénat, pp. 43−74, Clermont−Ferrand.

Maramaï, A., L. Graziani, G. Alessio, P. Burrato, L. Colini, L. Cucci, R. Nappi, A. Nardi, and G. Vilardo (2005) Near− and far−field survey report of the 30 December 2002 Stromboli (Southern Italy) tsunami, *Mar. Geol.*, *215*, 93–106.

Masson, D. G., A. B. Watts, M. J. R. Gee, R. Urgeles, N. C. Mitchell, T. P. Le Bas, and M. Canals (2002), Slope failures on the flanks of the western Canary Islands, *Earth Sc. Rev.*, *57*, 1–35.

McMurtry, G. M., P. Watts, G. J. Fryer, J. R. Smith, F. Imamura (2004), Giant landslides, mega−tsunamis, and paleo−sea level in the Hawaiian Islands, *Mar. Geol., 203*, 219–233, doi:10.1016/S0025−3227(03)00306−2.

Merle, O., and J.–F. Lénat (2003), Hybrid collapse mechanism at Piton de la Fournaise volcano, Réunion Island, Indian Ocean, *J. Geophys. Res., 108*(B3), 2166, doi:10.1029/2002JB002014.

Michon, L., and F. Saint−Ange (2008), Morphology of Piton de la Fournaise basaltic shield volcano (La Réunion Island): Characterization and implication in the volcano evolution, *J. Geophys. Res.*, *113*, B03203, doi:10.1029/2005JB004118.

Miller, D. J. (1960), The Alaska earthquake of July 10, 1958: Giant wave in Lituya Bay, *Bull. Seism. Soc. Am.*, *50 (2)*, 253–266.

Moore, J. G., and G. W. Moore (1984), Deposit from a giant wave on the island of Lanai, Hawaii, *Science, 226*, 1312–1315.

Moore, G. W., and J. G. Moore (1988), Large−scale bedforms in boulder gravel produced by giant waves in Hawaii. in *Sedimentologic consequences of convulsive geologic events*. Sp. Pap. Geol. Soc. Am., *229*:101–110.

Moore, J. G., D. A. Clague, R. T. Holcomb, P. W. Lipman, W. R. Normark, and M. E. Torresan (1989), Prodigious submarine landslides on the Hawaiian Ridge, *J. Geophys. Res.*, *94*, 17465–17484.

Moore, J. G., W. B. Bryan, K. R. Ludwig (1994), Chaotic deposition by giant wave, Molokai, Hawaii, *Geol. Soc. Am. Bull.*, *106*, 962–967.

Normark, W. R, J. G. Moore, and M. E. Torresan (1993), Giant volcano−related landslides and the development of the Hawaiian Islands. in US Geol. Surv. Bull. 2002, edited by W. C. Schwab, H. J. Lee, and D.C. Twichell, 184–196.

Oehler, J.–F., P. Labazuy, and J.–F. Lénat (2004), Recurrence of major flank landslides during the last 2−Ma−history of Réunion Island, *Bull. Volcanol.*, *66*, 585–598.

Oehler, J.–F., J. –F. Lénat, P. Labazuy (2007), Growth and collapse of the Réunion Island volcanoes, *Bull. Volcanol.*, *70*(6), 717–742, DOI 10.1007/s00445−007−0163−0.

Okal, E. A. and C. E. Synolakis (2003), A theoretical comparison of tsunamis from dislocations and landslides (2003), *Pure appl. geophys.*, *160*, 2177–2188, DOI 10.1007/s00024−003−2425−x.

Rançon, J. P. (1990), Lithostratigraphie du forage du Grand Brûlé. Implications volcanologiques. in *Le volcanisme de La Réunion*, edited by J.F. Lénat, pp 187–200, CRV, Clermont−Ferrand.

Ruff, L. J. (2003), Some aspects of energy balance and tsunami generation by earthquakes and landslides, *Pure Appl. Geoph.*, *160*, 2155–2176.

Sander, J., and K. Hutter (1996), Experimental and computational study of channelized water waves generated by a porous body, *Acta Mech.*, *91*, 119–155.

Synolakis, C. E., E. N. Bernard, V. V. Titov, U. Kanoglu, and F. I. Gonzalez (2008), Validation and verification of tsunami numerical models, *Pure Appl. Geophys.*, *165*, 2197–2228, doi:10.1007/s00024−004−0427−y.

Tinti, S., E. Bortolucci, and C. Romagnoli (1999), Modelling a possible holocenic landslide−induced tsunami at Stromboli volcano, Italy, *Phys. Chem. Earth*, *24*, 423–429.

Tinti, S., E. Bortolucci, and C. Romagnoli, (2000), Computer simulations of tsunamis due to sector collapse at Stromboli, Italy. *J. Volcanol. Geotherm. Res.*, *96*, 103–128.

Tinti, S., G. Pagnoni, and F. Zaniboni (2006a), The landslides and tsunamis of the 30th of December 2002 in Stromboli analysed through numerical simulations. *Bull. Volcanol.*, *68*, 462–479.

Tinti, S., A. Armigliato, A. Manucci, G. Pagnoni, F. Zaniboni, A. C. Yalçiner, Y. Altinok (2006b), The generating mechanism of the August 17, 1999 İzmit Bay (Turkey) tsunami: Regional (tectonic) and local (mass instabilities) causes, *Marine Geology*, *225*, 311–330.

Ward, S. N. (2001), Landslide tsunami, *J. Geophys. Res.*, *106* (*6*), 11,201–11,215.

Ward, S. N., and S. Day (2001), Cumbre Vieja Volcano – potential collapse and tsunami at La Palma, Canary Islands, *Geophys. Res. Lett.*, *28*, 3397–3400.

Watts, P., Imamura F., and Grilli S.T. (2000), Comparing model simulations of three benchmark tsunami generation cases, *Sci. Tsu. Haz.*, *18 (2)*, 107–123.

Waythomas, C. F., and P. Watts (2003), Numerical simulation of tsunami generation by pyroclastic flow at Aniakchak Volcano, Alaska, *Geophys. Res. Lett.*, *30* (*14*), 1751–1755, doi:10.1029/2003GL017220.

Waythomas, C. F., Watts, P., and J. S. Walder (2006), Numerical simulation of tsunami generation by cold volcanic mass flows at Augustine Volcano, Alaska, *Nat. Haz. Earth Syst. Sci.*, *6*, 671–685.

Waythomas, C. F., P. Watts, F. Shi, J. T. Kirby (2009), Pacific Basin tsunami hazards associated with mass flows in the Aleutian arc of Alaska *Quat. Sci. Rev.*, *28 (11−12)*, 1006–1019. doi: 10.1016/j.quascirev.2009.02.019.

Wei, G., J. T. Kirby, S. T. Grilli, R. Subramanya (1995), A fully nonlinear Boussinesq model for surface waves. Part 1. Highly nonlinear unsteady waves. *J. Fluid Mech.*, *294*, 71–92.

Figure Captions

Figure 1. (a) Map of debris avalanche deposits around Réunion Island (after Oehler et *al.*, 2007). Black circles indicate densely populated regions: SD = St Denis, LP = Le Port, Pa = St Paul, ES = Etang Salé, Pi =St Pierre, Ph = St Philippe, SR = Ste Rose, SB = St Benoît, SA = St André. Frames locate Figures 4 and 10. The coast is marked by the black line and the coastal shelf is the pale gray zone, encircled by a line, between the island and the avalanche deposits. (b) and (c) are 3D views focused on the frames that show the steep bathymetry of the island.

Figure 2. (a) Solid lines: 3D calculation of the elevation of water surface induced by a sudden displacement at the bottom for a flat topography. The volume displaced is 1 m^3 and water depth is respectively 25 m, 50 m and 100 m (the colored surface corresponds to the elevations obtained in Figure 2b). Points are calculated by equation (14). (b) 2D vertical slice of the 3D displacements. The water depth is 100 m. Arrow lengths are constant to allow visualization of small movements. Without 3D calculation, a displaced volume of 1 m^3 with the 1m×1m mesh size used would induce a very localized surface elevation of 1m (out of the graphic, central black line). (c) 3D−view of the surface elevation.

Figure 3. (a) Surface elevation obtained by 3D modeling (line) and equation (14) (points) for a volume of 1 m^3 displaced at the foot of a 45° talus (b). The water depth is 20 m. Fit is not exact but is clearly better than the 1m column obtained without correction. c) 3D−view of the surface elevation.

Figure 4. (a) Location of the simulated 10 km^3 and 25 km^3 landslides (the 25 km^3 landslide includes all the 10 km^3 area). The location of the figure is represented on Figure 1. (b) East/west outcrop showing the location of the geothermal drilling (* on Figure 4a). The numbers identify the 3 blocks used for a retrogressive scenario.

Figure 5. Thickness of computed landslide deposits obtained for scenarios 1 (a), 4 (b), 5 (c) and 6 (d). The pure constant retarding stress rheology (b) forms levées and well defined fronts as observed by Oehler et *al.* (2005) on natural deposits. The frictional rheology forms very spread out deposits with material accumulated as piles. Adding a water drag (a and d) conserves the characteristics of both rheologies even if the differences are less.

Figure 6. Water amplitude (m) generated by a 10 km^3 landslide at (a) t = 500 s (8.33 min), (b) 1000 s (16.66 min) and (c) 2500 s (41.66 min). Landslide deposits appear in dark.

Figure 7. Maximum water amplitude (m) generated by a 10 km^3 landslide (scenario 1). Note the amplitude increase over the ridge of the Mauritius Fracture Zone (x = 300, y = 100) and close to the shore. Axes are distances in km. The black contour indicates the shoreline. The white contour along the coasts indicates the area inundated by the tsunami. The curve draws the maximum water amplitude recorded along the west/east line. The circles locate the tide gauges of Figure 8.

Figure 8. Tide gauges of the numerical simulation (for a 10 km^3 landslide, scenario 1): (a) at Réunion Island, (b) at Mauritius and (c) in the ocean. The measurement for (a) and (b) is made off the coast (1 km distance) to avoid complex effects that may arise at the shore and that would not be taken into account by our depth−average approach. At the shore, the waves

slow down and, consequently, their amplitudes are higher than presented. See location in Figure 7.

Figure 9. (a) Maximum water amplitude generated by a landslide with a frictional behavior (φ_{bed} = 5°, V = 10 km^3, scenario 5). The submarine internal white contours indicate deposits thicker than 10 m. (b) Wave amplitudes at t = 500 s. The deposit simulated is the darker area, to the east of the island.

Figure 10. Waves generated by a submarine landslide of coastal platform a) west sliding, 2 km^3, b) northeast sliding, 0.5 km^3 and c) north sliding, 0.1 km^3. T = 20 kPa, C_f = 2, C_s = 0.01, no momentum transfer to water, resolution 200 m. The scale of amplitude of (a), (b) and (c) is different.
The graphics show the maximal wave amplitude along the shore (numbers indicate the distance in km from the bottom of the simulation domain)

Tables

Table 1. Main variables used

Table 2. Scenarios used for the simulation of the landslide from the active edifice

Table 3. Maximal wave amplitude (m) at different locations for various scenarios. Values in brackets indicate the amplitude of the first wave if it is not the highest wave. Locations are represented on Figure 7

Table 4. Time of arrival (in seconds) of the crest of the first wave at different locations for various scenarios. Locations are represented on Figure 7. Values in brackets indicate the duration of the sea level elevation preceding the crest

a)

N

0 10 20 km

Fig. 10

LP

SD

SA

Pa

SB

SR

ES

Pi

Ph

Fig. 4

topographic high

avalanches used
for the calibration
of the rheological model

S21°

S22°

E55°

E56°

Piton
de la Fournaise

S

N

W

topographic high

b)

Piton
de la Fournaise

S

N

W

coastal plateau

c)

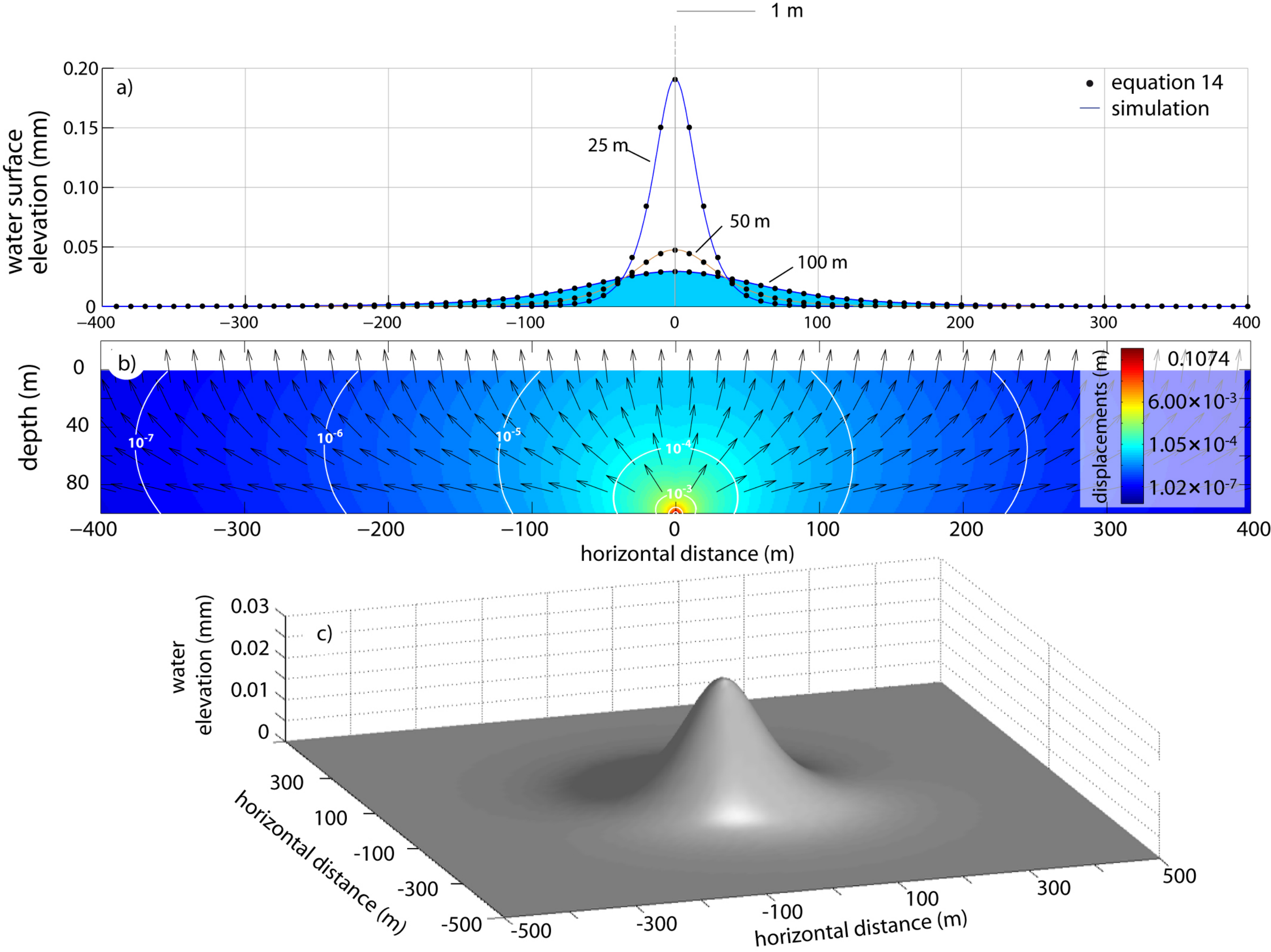
1 m
a)
equation 14
simulation
25 m
50 m
100 m
water surface elevation (mm)
0.20
0.15
0.10
0.05
0
−400
−300
−200
−100
0
100
200
300
400
b)
depth (m)
0
40
80
10^{-7}
10^{-6}
10^{-5}
10^{-4}
10^{-3}
displacements (m)
0.1074
6.00×10^{-3}
1.05×10^{-4}
1.02×10^{-7}
horizontal distance (m)
c)
water elevation (mm)
0.03
0.02
0.01
0
horizontal distance (m)
300
100
-100
-300
-500
horizontal distance (m)
-500
-300
-100
100
300
500

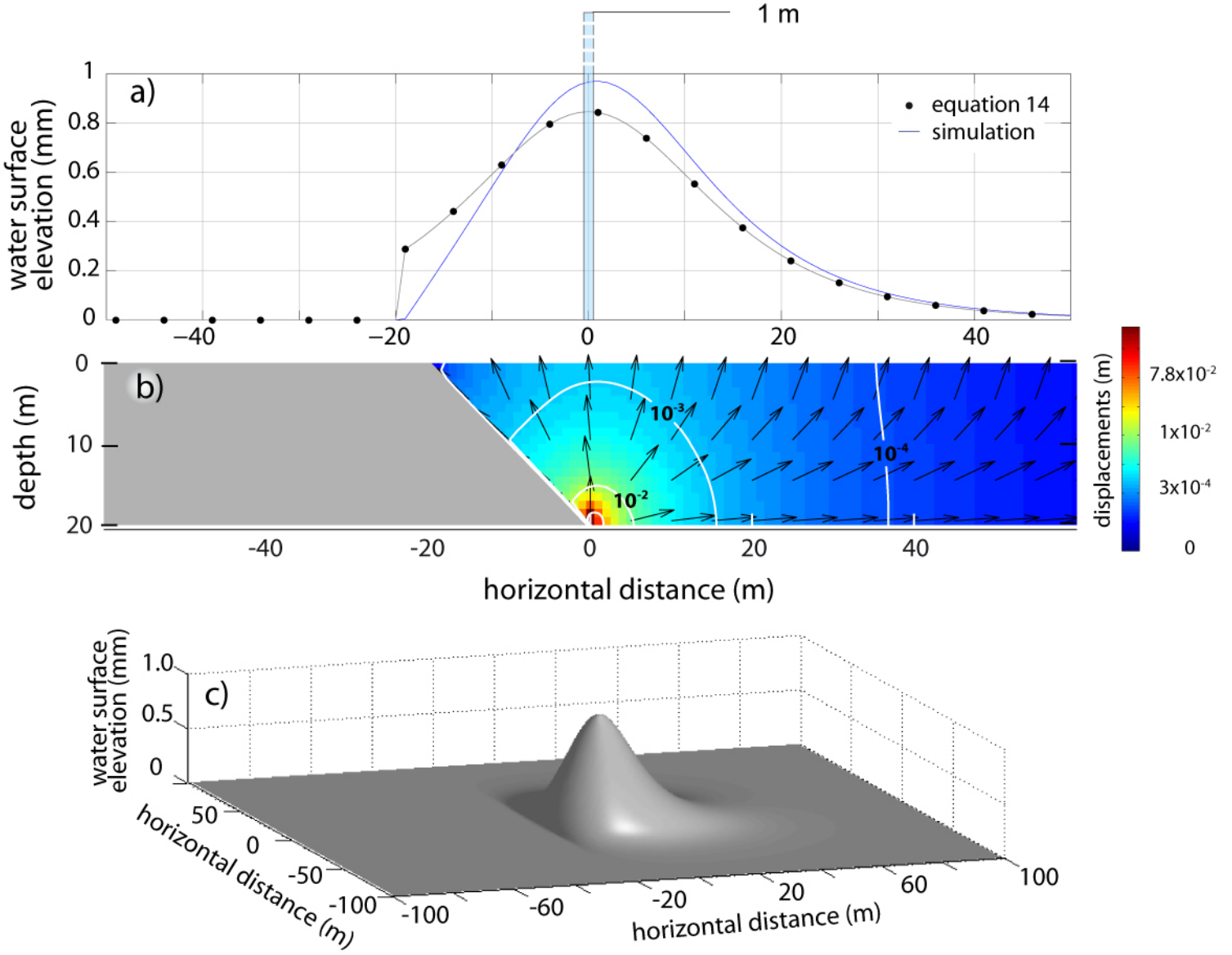
1 m
a)
water surface elevation (mm)
equation 14
simulation
b)
depth (m)
10^{-3}
10^{-4}
10^{-2}
displacements (m)
7.8x10^{-2}
1x10^{-2}
3x10^{-4}
0
horizontal distance (m)
c)
water surface elevation (mm)
horizontal distance (m)
horizontal distance (m)

summit of
Piton de la Fournaise
25 km³
10 km³
destabilization
2000
1500
1000
500
Indian Ocean
a)
Northing (km)
Easting (km)
0
10
20
30
40
50
60
70
Geothermal
drilling
10 km³ destabilization
3
2
1
Indian Ocean
b)
Elevation (m)
1500
1000
500
0
-500
-1000
10
15
20
Easting (km)

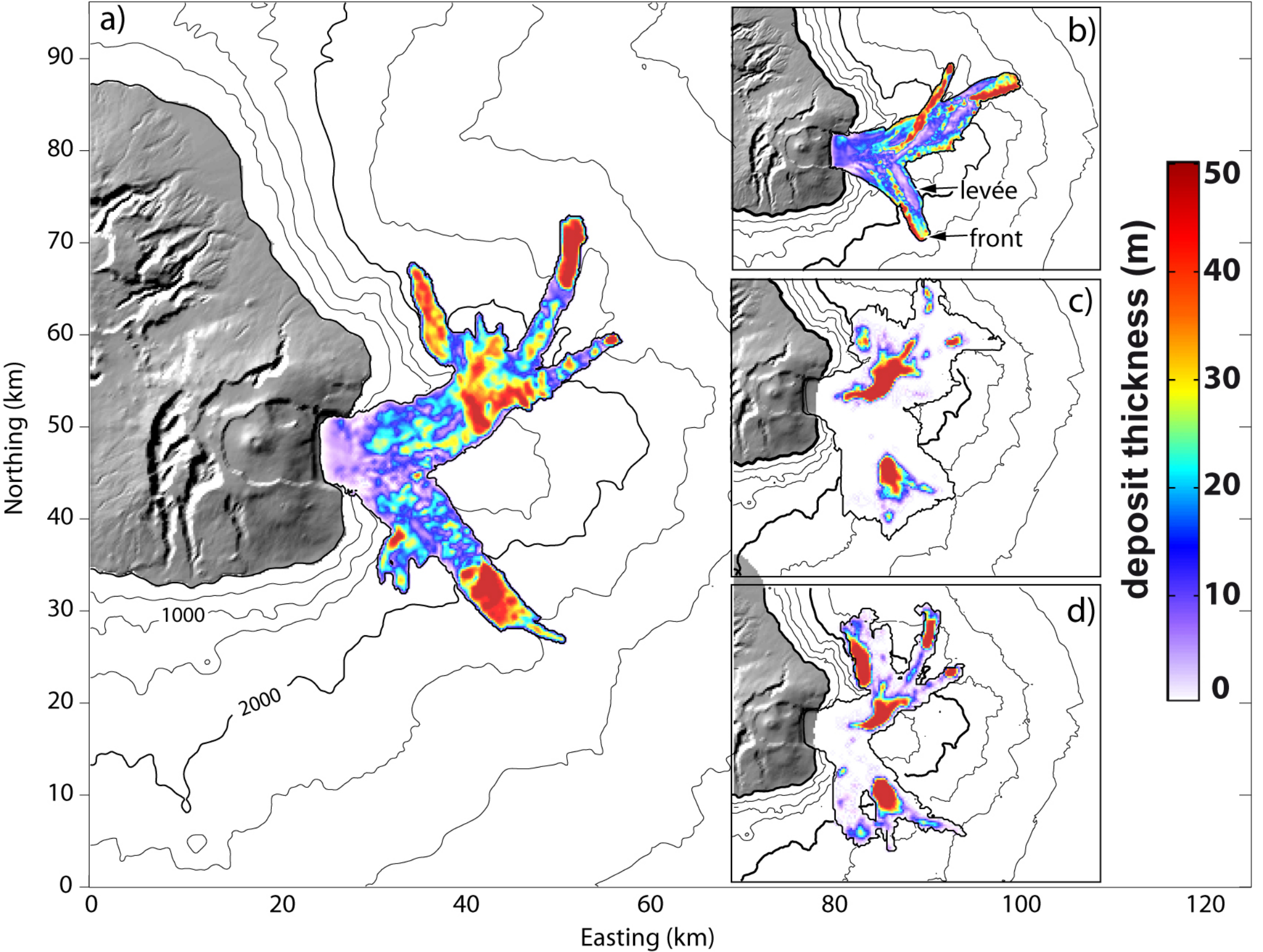
a)
b)
c)
d)
levée
front
1000
2000
Northing (km)
Easting (km)
0
10
20
30
40
50
60
70
80
90
0
20
40
60
80
100
120
deposit thickness (m)
50
40
30
20
10
0

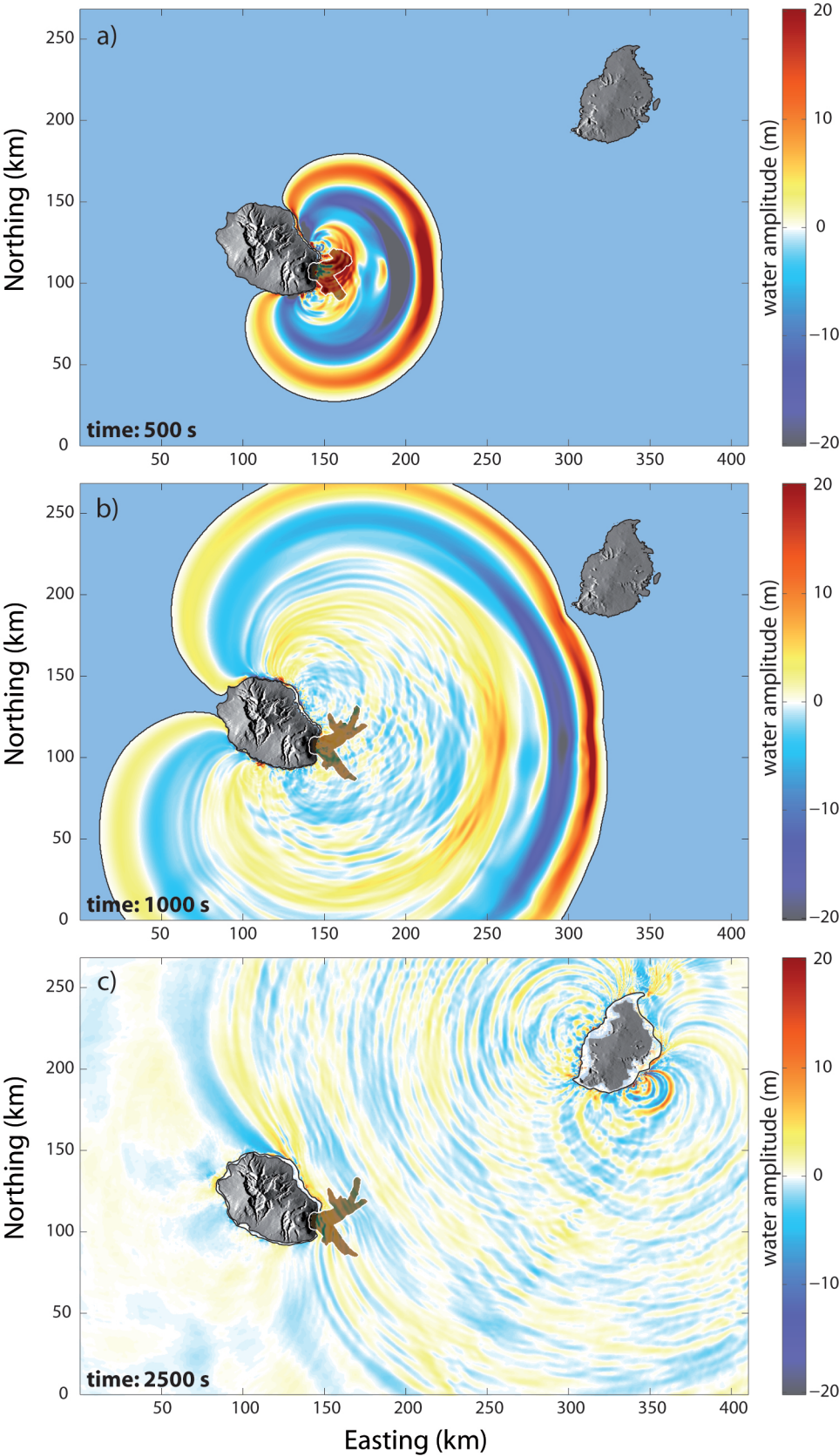
a)
time: 500 s
b)
time: 1000 s
c)
time: 2500 s
Northing (km)
Easting (km)
water amplitude (m)
0
50
100
150
200
250
300
350
400
20
10
−10
−20

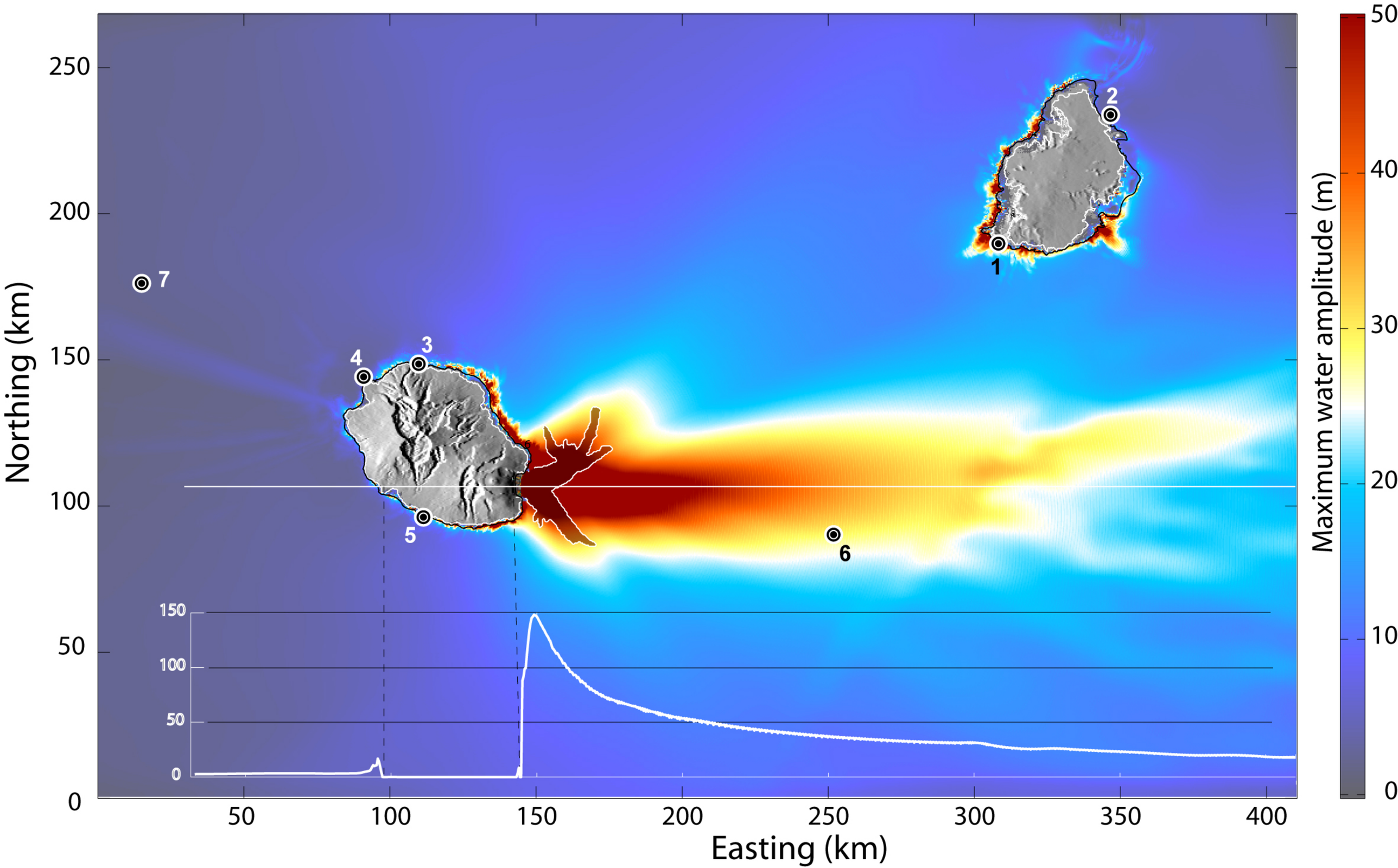
Northing (km)
Easting (km)
Maximum water amplitude (m)
0
50
100
150
200
250
300
350
400
10
20
30
40
1
2
3
4
5
6
7

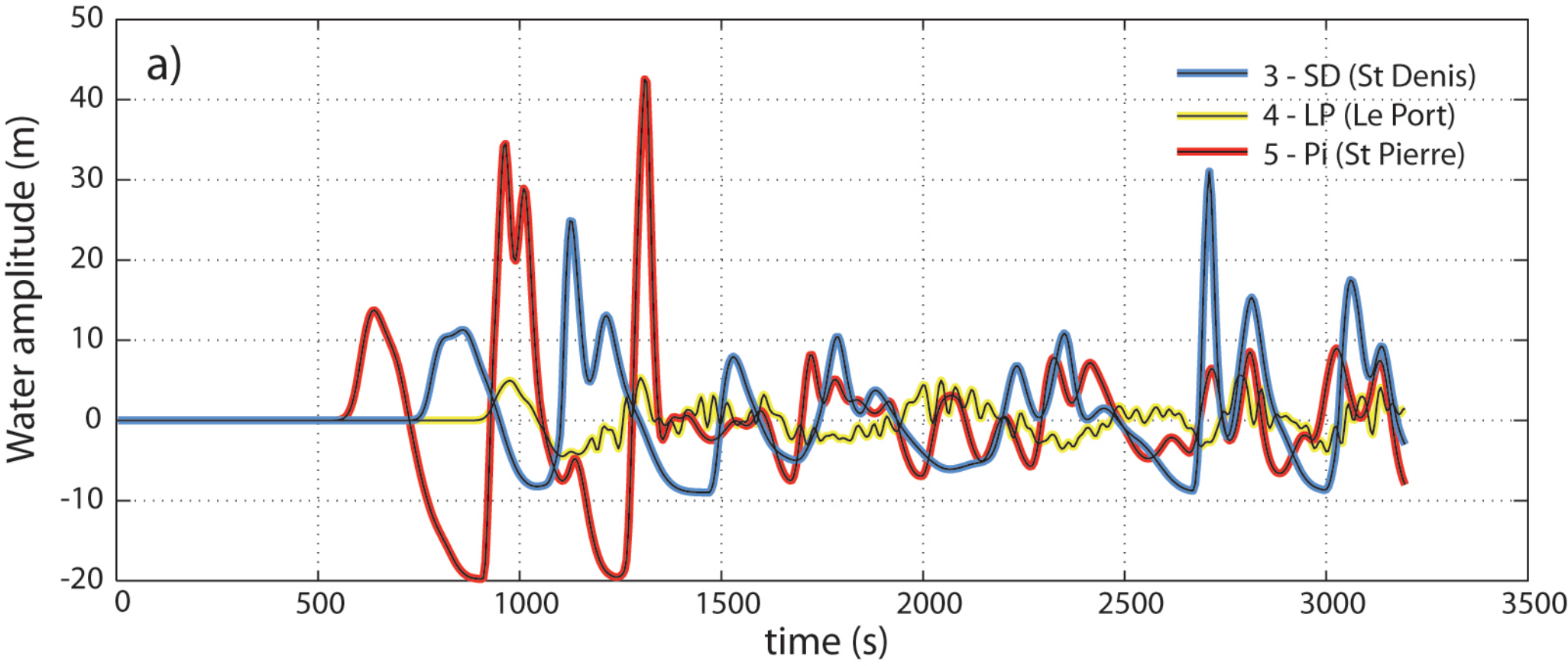
a)
3 - SD (St Denis)
4 - LP (Le Port)
5 - Pi (St Pierre)
Water amplitude (m)
time (s)
50
40
30
20
10
0
-10
-20
0
500
1000
1500
2000
2500
3000
3500

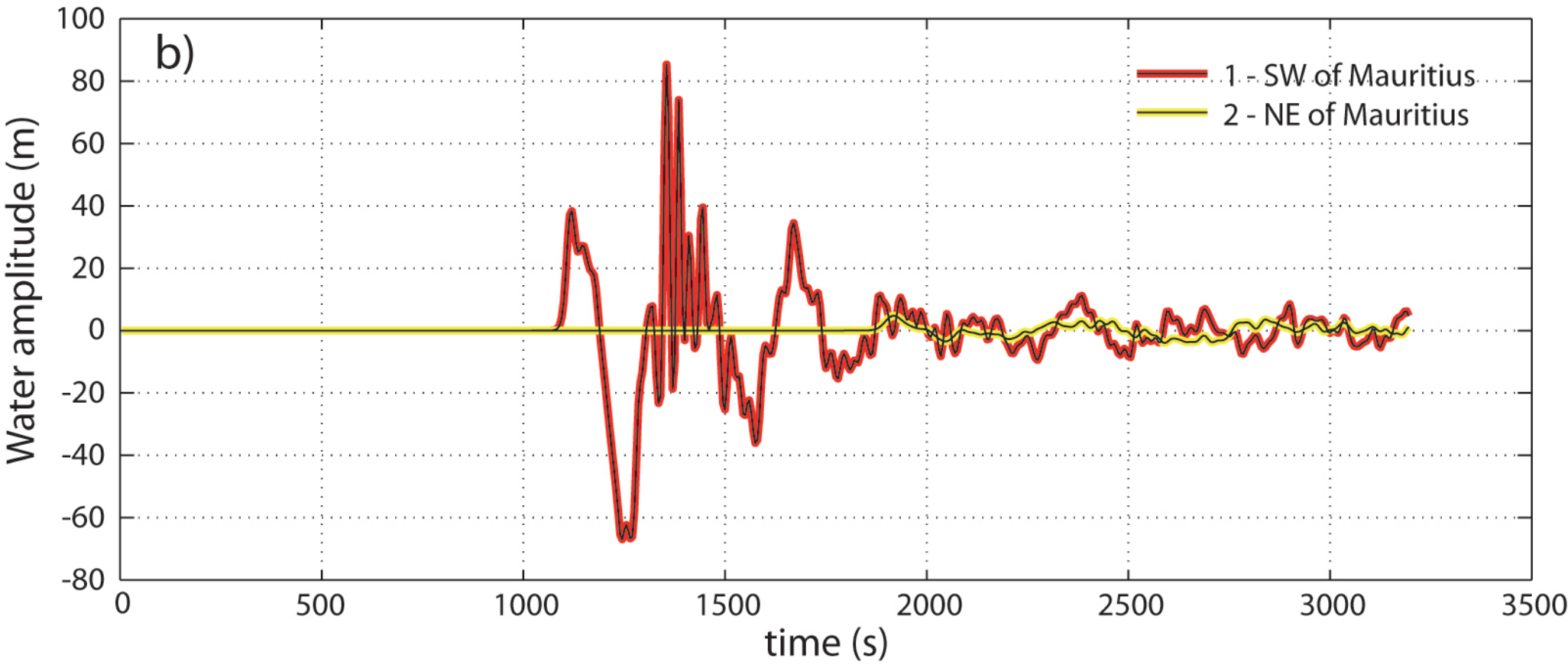
b)
1 - SW of Mauritius
2 - NE of Mauritius
Water amplitude (m)
time (s)
100
80
60
40
20
0
-20
-40
-60
-80
0
500
1000
1500
2000
2500
3000
3500

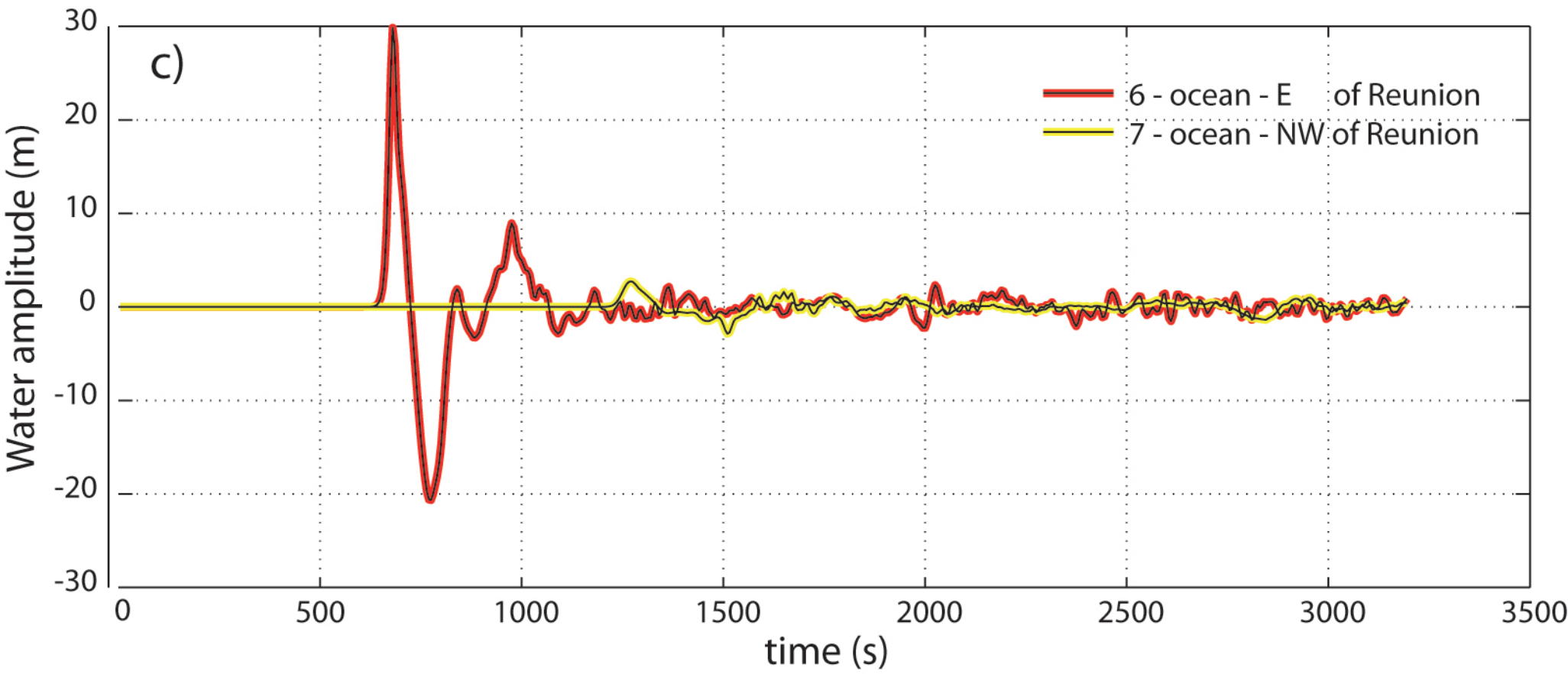
c)
6 - ocean - E of Reunion
7 - ocean - NW of Reunion
Water amplitude (m)
time (s)
30
20
10
0
-10
-20
-30
0
500
1000
1500
2000
2500
3000
3500

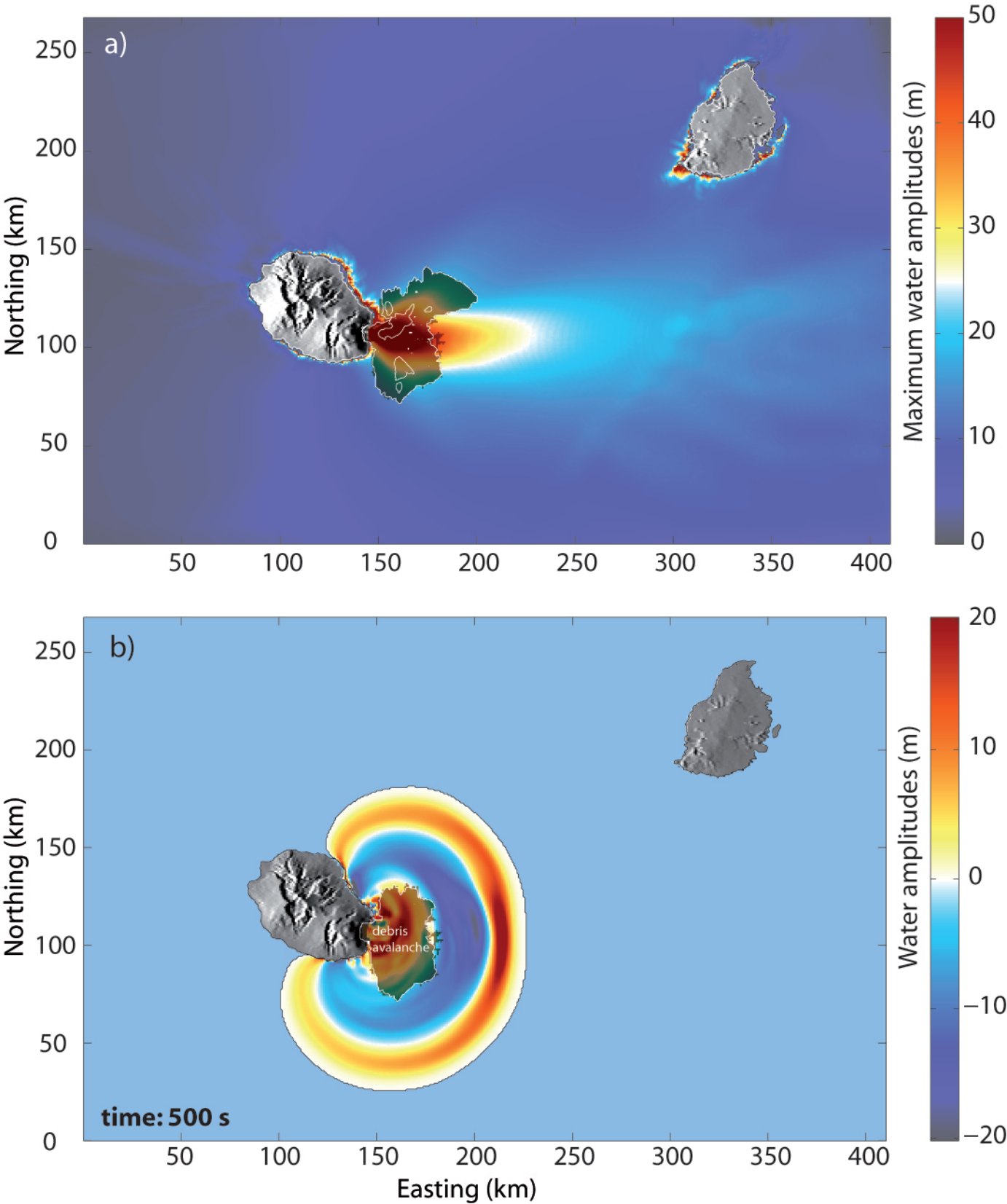
a)
b)
Northing (km)
Easting (km)
Maximum water amplitudes (m)
Water amplitudes (m)
debris avalanche
time: 500 s
0
50
100
150
200
250
300
350
400
−10
−20
10
20
30
40

a
b
c
coastal plateau
deposit
SP
LP
SD
wave amplitude (m)
distance along the shore (km)
70 km
60 km
40 km
30 km
20 km
Northing (km)
Easting (km)
Maximum water amplitude (m)

Table 1.

symbol	variable	unit
C_f	frontal drag coefficient	dimensionless
C_s	surface drag coefficient	dimensionless
g	gravity	m s^{-2}
h_a	landslide thickness	m
h_w	water depth	m
$k_{act/pass}$	earth pressure coefficient	dimensionless
z	fixed topography elevation	m
z_w	water surface elevation	m
Δz	variation of water surface elevation	m
$\mathbf{R} = (R_x, R_y)$	stress exerted by the landslide on the water	Pa
$\mathbf{T} = (T_x, T_y)$	retarding stress of the landslide	Pa
$\mathbf{u} = (u_x, u_y)$	landslide velocity	m s^{-1}
$\mathbf{v} = (v_x, v_y)$	water velocity	m s^{-1}
V	volume	m^3
α	slope of the fixed topography	degrees
β	slope of the ocean bottom (fixed topography + landslide)	degrees
μ_w	water dynamic viscosity	Pa s
ρ_a	landslide density	kg m^{-3}
ρ_w	water density	kg m^{-3}
ρ	relative density of the landslide, $\rho = \rho_a - \rho_w$	kg m^{-3}
χ	attenuation coefficient	dimensionless

Table 2.

Scenario	Volume (km^3)	type of collapse	Model	Value	C_s	C_f	momentum transfer to water
1	10	single	constant stress	20 kPa	0.01	2	no
2	10	single	constant stress	20 kPa	0.01	2	yes
3	10	single	constant stress	35 kPa	0.005	1	no
4	10	single	constant stress	50 kPa	0	0	no
5	10	single	frictional	5°	0	0	no
6	10	single	frictional	3°	0.01	2	no
7	25	single	constant stress	20 kPa	0.01	2	no
8	10	retrogressive	constant stress	20 kPa	0.01	2	no

Table 3.

Scenario	SW of Mauritius point 1	NE of Mauritius point 2	St Denis point 3	Le Port point 4	St Pierre point 5	Ocean−W point 6	Ocean−E point 7
1	85 (38)	5	31 (11)	5.5 (5)	42 (14)	2.7	30
2	75 (60)	7.5 (7)	28 (15)	9 (7)	36 (18)	3.8	46
3	76	12	31	5.5	40	2.8	35
4	70 (65)	9 (6)	30 (10)	6 (5)	56 (12)	2.7	49
5	88 (30)	3.5	36 (10)	4 (3)	14	1.7	19
6	62 (37)	11 (5)	27 (13)	7 (5.5)	39 (15)	2.7	30
7	128	18 (14)	34 (23)	16	41 (29)	11	113
8	30 (18)	5 (2)	19 (4.5)	5.5 (1.6)	37 (4)	1.5 (1.0)	25 (15)

Table 4.

Scenario	SW of Mauritius point 1	NE of Mauritius point 2	St Denis point 3	Le Port point 4	St Pierre point 5	Ocean−W point 6	Ocean−E point 7
1	1120 (30)	1920 (60)	860 (120)	975 (75)	635 (75)	1270 (50)	680 (30)
2	1110 (30)	1905 (25)	845 (95)	975 (75)	635 (75)	1260 (30)	670 (25)
3	1115 (55)	1910 (60)	845 (125)	975 (70)	635 (85)	1265 (50)	675 (35)
4	1100 (25)	1890 (50)	810 (60)	965 (65)	635 (85)	1260 (50)	665 (40)
5	1125 (60)	1910 (95)	810 (95)	985 (100)	1005 (85)	1275 (60)	685 (70)
6	1120 (40)	1915 (50)	860 (110)	975 (75)	635 (70)	1275 (60)	680 (40)
7	1100 (20)	1895 (45)	790 (50)	970 (60)	620 (55)	1260 (140)	670 (30)
8	1120 (45)	1915 (50)	810 (70)	960 (60)	620 (70)	1255 (50)	685 (50)